An InSAR Ionospheric Correction Method Based on Variance Component Estimation With Integration of MAI and RSS Measurements

Wenfei Mao, Guoxiang Liu, Xiaowen Wang, Rui Zhang, Wei Xiang, Shuaiying Wu, Bo Zhang, Jiawen Bao, Jialun Cai, and Saeid Pirasteh

***Abstract*—Ionospheric phase delay can seriously affect the low-frequency spaceborne synthetic aperture radar (SAR) systems. Ionospheric correction is, therefore, vital to improving the measurement accuracy of Interferometric SAR (InSAR). InSAR ionospheric correction relies mainly on two kinds of approaches, i.e., one uses SAR azimuth offsets measures, and the other achieves through a range split-spectrum (RSS) technique. However, the two approaches have different spatial sensitivities to the ionosphere, but they can complement each other. In this study, we present an integration InSAR ionospheric correction method. This method uses the Helmert variance component estimation to reasonably allocate the weights for the ionospheric measurements obtained from the azimuth offset-based and RSS techniques to improve the ionospheric correction performance. The azimuth offset can be derived from a pixel offset-tracking procedure or multiple-aperture InSAR. We demonstrated the proposed method on 28-MHz FBS mode ALOS-1 PALSAR images acquired before and after the Wenchuan earthquake in Sichuan Province, China, 2008. This study also applied the proposed method to 14-MHz FBD mode ALOS-1 PALSAR images with no significant surface deformation and high coherence in Chile. After the ionospheric correction with the proposed method, we found that the ionospheric errors in the Wenchuan and Chile cases have varied from −31.0 to 21.1 cm and −4.7 to 93.9 cm, respectively. The results show that the proposed method can effectively remove the long-wavelength ionospheric delay. Our study reveals that this method can also alleviate the influence of local ionospheric disturbance simultaneously.**

***Index Terms*—Interferometric synthetic aperture radar (InSAR), Helmert variance component estimation (H-VCE), range split-spectrum (RSS), SAR azimuth offset.**

I. Introduction

INTERFEROMETRIC synthetic aperture radar (InSAR) has been widely used to measure ground deformation related to glacier movements, landslides, earthquakes, land subsidence, and volcanic eruptions [1]–[11]. However, the accuracy of InSAR measurement is strongly affected by the spatiotemporal decorrelation of SAR signals. This accuracy may result from the distortion of SAR imaging geometry, significant surface topographic changes, and atmospheric phase delay [12]. The ionosphere, which distributes 60–1000 km away from the earth's surface as a part of the atmosphere, is one of the primary error sources for InSAR measurements. Correcting for ionospheric phase delay is especially critical to SAR sensors' measurements operating in low-frequency microwave bands, such as the *L*-band and *P*-band sensors [13].

Several methods existed to correct ionospheric phase delay [14]–[29] in InSAR measurements. These methods can be simply divided into following four categories:

1) range group-phase delay method [14];
2) Faraday rotation method [15]–[19];
3) azimuth offset-based method [20]–[23]; and
4) range split-spectrum (RSS) method [24]–[29].

The range group-phase delay method exploits the range shift between SAR images caused by ionospheric perturbation and, then, estimates the ionosphere's phase delay. The range group-phase delay method's accuracy is closely related to the SAR images' coregistration quality in the range direction. The current *L*-band SAR sensors (e.g., ALOS-1/2), however, commonly have low range resolutions [12], and thus, it is limiting the application of the range group-phase method. The Faraday rotation method can obtain absolute ionospheric total electron content (TEC) from the full-polarization SAR images and, then, calculate the expected phase delay of the ionosphere [25]. However, this method highly depends on the accuracy of the earth's magnetic field [25]. Among the four methods earlier, the azimuth offset-based and the RSS methods are, therefore, the most commonly used approaches to ionospheric phase delay correction over the past years.

The azimuth offset-based method relies on the estimated SAR azimuth offsets, which can be obtained from the SAR intensity offset tracking or the multiaperture interferometry (MAI) technique [21], [22]. Integrating the estimated azimuth offsets along the SAR azimuth direction can then address the ionospheric phase delay. This method can estimate the ionosphere spectrum's high-frequency components but is prone to induce significant errors over long distances because the estimation

Manuscript received October 12, 2020; revised November 30, 2020; accepted December 13, 2020. Date of publication December 16, 2020; date of current version January 6, 2021. This work was supported in part by the National Key R&D Program of China under Grant 2017YFB0502700, in part by the National Natural Science Foundation of China under Grant 41771402, Grant 41804009, and Grant 42071410, and in part by the Cultivation Program for the Excellent Doctoral Dissertation of Southwest Jiaotong University. *(Corresponding authors: Xiaowen Wang; Guoxiang Liu.)*

The authors are with the Department of Surveying and Geo-Informatics, Faculty of Geosciences and Environmental Engineering, Southwest Jiaotong University, Chengdu 610031, China (e-mail: wenfei192912@163.com; rsgxliu@swjtu.edu.cn; insarwxw@gmail.com; zhangrui@swjtu.edu.cn; xw_swjtu@foxmail.com; shining@my.swjtu.edu.cn; rsbozh@gmail.com; durahan21023@gmail.com; caijialunmail@foxmail.com; sapirasteh@swjtu.edu.cn).

Digital Object Identifier 10.1109/JSTARS.2020.3045267

involves integration processing [30]. Moreover, the azimuth offset-based method is insensitive to ionospheric variations along the SAR range direction. The RSS method divides the range spectrum of the SAR image into two subbands, forming two SAR images with different center frequencies. We then used the subband images to generate two subband interferograms. The RSS method then exploits the phase difference between the two subband interferograms to retrieve the InSAR phase's dispersive component, referred to as the ionospheric phase delay [30], [31]. The RSS method can accurately extract ionospheric long-wavelength variations and effectively recover range variations [30]. However, the RSS method generally needs spatial filtering with a large window size to the average SAR phase due to the narrow range bandwidth of current *L*-band SAR systems, which may lead directly to the masking out of small-scale ionospheric phase variations [32].

From the previous descriptions, both the azimuth offset-based method and the RSS method have their advantages, and none of them can comprehensively remove the ionospheric phase delay. To benefit the two methods in ionospheric correction, Gomba *et al.* in 2017 proposed the Bayesian combination method [25]. They assumed that the ionosphere could be represented by a single thin layer with known height and used a power-law spectral density function to simulate ionospheric phase as *a priori* information [25]. The simulated ionospheric phase was then employed to invert real ionospheric phase with a Bayesian inverse method [25]. Although this method has shown good performance for correcting small-scale variations in the ionospheric aurora effect and equatorial scintillation event [25], its accuracy highly depends on the simulated *a priori* information. The performance of the correction may degrade due to the complex spatiotemporal characteristics of the ionosphere.

Given that the azimuth offset-based and RSS methods complement each other, in this study, we proposed an approach to integrate the two techniques to improve the performance of InSAR ionospheric component correction. We employed a Helmert variance component estimation (H-VCE) algorithm to reasonably allocate the weights for the ionospheric measurements from the azimuth offset (MAI)-based and RSS methods. The integrated method enables us to take advantage of the two preexisting methods in a straightforward way. We tested the proposed method on two datasets of ALOS PALSAR images covering the 2008 Wenchuan earthquake, China, and a coastal area in Chile, respectively, each with different characteristics. This study shows how the proposed approach can improve the estimate of coseismic deformation with strong ionospheric disturbances. In contrast to the Wenchuan case, Chile's test area has no evident ground deformation to better demonstrate the proposed method's correction accuracy.

II. Methodology

A. Estimating Ionospheric Phase Using SAR Azimuth Offsets

The azimuth-offset-based method exploits the rationale that the interferometric phase gradient along the SAR azimuth direction caused by the ionosphere ($\Delta\phi_{\mathrm{ion\_Azi}}/\Delta_{\mathrm{az}}$) is linearly proportional to the azimuth offsets Δx between one SAR image pair [10]

$$\frac{\Delta\phi_{\mathrm{ion\_Azi}}}{\Delta_{\mathrm{az}}} = \alpha \cdot \frac{4\pi}{\lambda} \cdot \Delta x + \beta \tag{1}$$

where *x* and *r* are the line and column indexes, respectively, $\Delta\phi_{\mathrm{ion\_Azi}} = \Delta\phi_{\mathrm{ion\_Azi}}(x+1,r) - \Delta\phi_{\mathrm{ion\_Azi}}(x,r)$, Δ_{az} is the azimuth pixel spacing of the interferogram, λ is the radar wavelength, α is a factor related to the parameters of the SAR system, and β is an offset constant introduced by the reference point.

Here, we estimated SAR azimuth offset from the MAI technique. MAI uses a split-beam InSAR processing that generates forward- and backward-looking interferograms. The forward- and backward-looking interferograms are then multiplied by conjugate to obtain the final MAI interferogram. The relationship between SAR azimuth offset and MAI phase (ϕ_{MAI}) is [21], [22]

$$\Delta x = -\frac{l}{4\pi n} \cdot \phi_{\mathrm{MAI}} \tag{2}$$

where *l* is the effective antenna length of the SAR sensor, and *n* is a normalized squint that is a fraction of the full aperture width.

According to (1) and (2), we can calculate the ionospheric phase $\phi_{\mathrm{ion\_Azi}}$ through an integration of the phase gradient along the SAR azimuth direction

$$\phi_{\mathrm{ion\_Azi}} = \sum_{u=1}^{x} \left[\left(-\alpha \cdot \frac{l}{\lambda n} \cdot \phi_{\mathrm{MAI}}(u,r) + \beta \right) \cdot \Delta_{\mathrm{az}} \right] + C \tag{3}$$

where *C* is the integral constant that varies with the range position, whose estimation methods are presented in [21] and [22]. The parameters α and β can be determined by a polynomial fitting using the pixels with high coherences and no large surface deformation.

B. Estimating Ionospheric Phase Using the RSS Technique

The interferometric phase of the SAR interferogram disturbed by the ionosphere can be divided into two parts: the nondispersive and dispersive phases. The dispersive phase component is referred to as the ionospheric phase ($\phi_{\mathrm{ion\_Rss}}$), i.e.,

$$\phi_0 = \phi_{\mathrm{ion\_Rss}} + \phi_{\mathrm{nondisp}}. \tag{4}$$

The RSS method separates the nondispersive phase from the dispersive phase by exploiting the two components' different frequency behavior. The procedure consists of the generation of two range subband images with varying frequencies of center f_{L} (lower frequency) and f_{H} (higher frequency) using a band-pass filtering processing. Two subband interferograms are then formed from one image pair using the subband SAR images, whose interferometric phase (ϕ_{L} and ϕ_{H}) can be expressed as [24], [25]

$$\begin{cases} \phi_{\mathrm{L}} = \phi_{\mathrm{nondisp}} \cdot \frac{f_{\mathrm{L}}}{f_0} + \phi_{\mathrm{ion\_Rss}} \cdot \frac{f_0}{f_{\mathrm{L}}} \\ \phi_{\mathrm{H}} = \phi_{\mathrm{nondisp}} \cdot \frac{f_{\mathrm{H}}}{f_0} + \phi_{\mathrm{ion\_Rss}} \cdot \frac{f_0}{f_{\mathrm{H}}} \end{cases} \tag{5}$$

where f_0 represents the radar center frequency. From (4) and (5), we can estimate $\phi_{\mathrm{ion\_Rss}}$ through a linear combination of

ϕ_0 and $(\phi_{\rm H} - \phi_{\rm L})$

$$\phi_{\rm ion\_Rss} = \frac{f_{\rm L} f_{\rm H}}{f_0^2 + f_{\rm L} f_{\rm H}} \cdot \left[\phi_0 - \frac{f_0}{(f_{\rm H} - f_{\rm L})} \cdot (\phi_{\rm H} - \phi_{\rm L})\right]. \tag{6}$$

C. Integrating the Offset-Based and RSS Methods Using H-VCE

As mentioned in Section I, the SAR azimuth offset-based and RSS methods, which have their advantages and limitations, complement each other. Attempts of combing these two methods have been conducted using *a priori* information from a power-law spectral density function [25]. Unfortunately, such *a priori* information is difficult or even impossible to be accurately simulated due to the ionospheric complex nature [33]. Here, we introduced a new technique by integrating the two methods for improving the InSAR ionospheric correction. We regarded the ionospheric estimates from two methods as two groups of independent observations and constructed a model by relating the ionospheric phase to the differential TEC (DTEC, $\Delta_{\rm TEC}$) between the primary and secondary images

$$\begin{cases} \underset{m\times 1}{\phi_{\rm ion\_Azi}} = \underset{m\times m}{B_{\rm Azi}} \cdot \underset{m\times 1}{\Delta_{\rm TEC}} + \underset{m\times 1}{\delta_{\rm Azi}} \\ \underset{m\times 1}{\phi_{\rm ion\_Rss}} = \underset{m\times m}{B_{\rm Rss}} \cdot \underset{m\times 1}{\Delta_{\rm TEC}} + \underset{m\times 1}{\delta_{\rm Rss}} \end{cases} \tag{7}$$

where $\phi_{\rm ion\_Azi}$ and $\phi_{\rm ion\_Rss}$ are the ionospheric phase vectors derived from the azimuth offset-based and RSS methods, respectively, *m* represents the dimension of the ionospheric phase vector $B_{\rm Azi} = B_{\rm Rss} = {\rm diag}[(4\pi K)/(c \cdot f_0)]_{m\times m}$, $K = 40.28$ ($\rm m^3/s^2$), $\delta_{\rm Azi}$ and $\delta_{\rm Rss}$ are the errors of the estimates from the two methods, respectively.

We took the ionospheric phase estimated by the azimuth offset-based method as the first group of observation, and these from the RSS method as the second group. We then resolved (7) by employing the H-VCE algorithm, which has been extensively used to determine the relative weights between different groups of observations whose *a priori* uncertainties are unknown [33], [34]. The H-VCE algorithm employs an iteration procedure to calculate and update each observation group's unit weight variance, from which the optimal relative weights are determined.

To make it easier to be understood, we rewrite (7) as an error equation

$$V = B \cdot \Delta_{\rm TEC} - L \tag{8}$$

where *L*, *B*, and *V* represent the observations, transfer matrix, and corrected results, respectively, i.e.,

$$L = [\phi_{\rm ion\_Azi}, \phi_{\rm ion\_Rss}]^{\rm T},\ \ B = [B_{\rm Azi}, B_{\rm Rss}]^{\rm T},\ \ V = [v_1, v_2]^{\rm T} \tag{9}$$

where v_1 and v_2 represent the correction vectors of $\phi_{\rm ion\_Azi}$ and $\phi_{\rm ion\_Rss}$, respectively.

The H-VCE algorithm does not require precise initial weights of the observations. Therefore, we determined the initial weights by using the variances of $\phi_{\rm ion\_Azi}$ and $\phi_{\rm ion\_Rss}$, i.e., the initial weights of $\phi_{\rm ion\_Azi}$ and $\phi_{\rm ion\_Rss}$ are $P_{01} = 1/{\rm var}(\phi_{\rm ion\_Azi})$ and $P_{02} = 1/{\rm var}(\phi_{\rm ion\_Rss})$, respectively. With (8) and (9), we can estimate the unknown DTEC ($\Delta_{\rm TEC}$) with a weighted least squares method

$$\Delta_{\rm TEC} = N^{-1} W \tag{10}$$

where $N = N_1 + N_2$, $N_1 = B_{\rm Azi}^{\rm T} P_1 B_{\rm Azi}$, $N_2 = B_{\rm Rss}^{\rm T} P_2 B_{\rm Rss}$, and $W = W_1 + W_2$, $W_1 = B_{\rm Azi}^{\rm T} P_1 \phi_{\rm ion\_Azi}$, $W_2 = B_{\rm Rss}^{\rm T} P_2 \phi_{\rm ion\_Rss}$.

Considering the low computational efficiency of the H-VCE rigorous algorithm, we adopted its simplified algorithm to calculate the unit weight variance of each observation group, i.e.,

$$\begin{cases} \hat{\sigma}_1^2 = \frac{v_1^{\rm T} P_1 v_1}{m - {\rm tr}(N^{-1} N_1)} \\ \hat{\sigma}_2^2 = \frac{v_2^{\rm T} P_2 v_2}{m - {\rm tr}(N^{-1} N_2)} \end{cases} \tag{11}$$

where $\hat{\sigma}_1^2$ and $\hat{\sigma}_2^2$ are the unit weight variances of $\phi_{\rm ion\_Azi}$ and $\phi_{\rm ion\_Rss}$, respectively.

After the estimation of unit weight variances for observation groups $\phi_{\rm ion\_Azi}$ and $\phi_{\rm ion\_Rss}$, we can update the weight matrices for the two groups through

$$\hat{P}_j = \hat{\sigma}_1^2 P_{0j} / \hat{\sigma}_j^2 \ (j = 1, 2)\,. \tag{12}$$

The proposed method's main implementation steps are as follows.

1) Using the coherence coefficients of $\phi_{\rm ion\_Azi}$ and $\phi_{\rm ion\_Rss}$ to determine the initial weights of the two groups of observation, i.e., P_{01} and P_{02}, and calculate their initial unit weight variances.
2) Using (10) to calculate the initial DTEC ($\Delta_{\rm TEC}$).
3) Using (8) to obtain the two group observations' residuals and, then, using the obtained residuals to calculate their unit weight variances with (11).
4) Using (12) to update the weights of the observations.
5) Using the reupdated weights and (8) to calculate the residuals again.
6) Repeating steps (3) to (5) until $|\hat{\sigma}_1^2 - \hat{\sigma}_2^2| < 10^{-3}$ and the weight matrices from the final iteration are used to calculate $\Delta_{\rm TEC}$, which is then converted into ionospheric phase delay.

The estimated ionosphere phase is finally subtracted from the original SAR interferogram to obtain the corrected InSAR measurements. Fig. 1 shows the main processing flow of the proposed method.

III. Experimental Results

Table I lists the SAR images used in this study for verification of our proposed method. The ALOS PALSAR images, acquired along the paths of 471 and 103, comprise nine adjacent frames from frame 570 to 650 and seven adjacent frames from frame 6700 to 6760, respectively. Path 471 covers the eastern part of the rupturing fault of the Wenchuan earthquake with a central location of 105.6 °E, 31.7 °N [see Fig. 2(a)]. The Wenchuan earthquake occurred on a reverse fault and ruptured about 400 km, releasing a vast moment equivalent to Mw 7.9. The sensing dates for primary and secondary images are 29th February and 31st May in 2008, respectively, for the Wenchuan study site.

In contrast, the PALSAR images of path 103 cover the northern part of Chile [see Fig. 2(b)], where no significant deformation

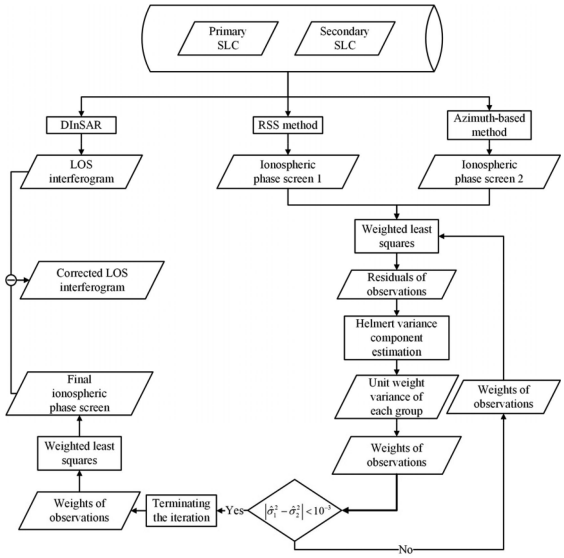

Fig.1. Flowchart processing of the combination method.

TABLE I
SAR IMAGES USED IN THIS STUDY

Track	Frame	Date	Mode	Perpendicular Baseline (m)	Temporal Baseline (d)
471	570-650	20080229 20080531	FBS	75	92
103	6700-6760	20070829 20071014	FDS	-354	46

occurred during the periods of SAR imaging (i.e., between 29th August and 14th October in 2007). The shuttle radar topography mission digital elevation model with a spatial resolution of 30 m was used to remove the topographic phase in the interferograms. We used commercial GAMMA software to process the PALSAR images [32].

A. Wenchuan Earthquake Test Case

Using (2), we obtained the azimuth displacement from the MAI interferogram. For the MAI interferogram generation, we adopted a normalized squint of 0.5 in (1). We applied 12 looks in range and 30 looks in azimuth to the MAI interferogram to reduce phase noise, followed by a phase smoothing with a Goldstein phase filter with a window size of 32 [36]. We also implemented the multilooking and phase filtering to the InSAR interferogram by adopting the same MAI processing parameters. All the interferograms were unwrapped by the minimum cost flow algorithm [37].

Based on (1), we estimated the system-dependent parameters α and β with a linear fitting method. Before the estimation, the MAI and InSAR interferograms were both masked using a coherence threshold of 0.4. This mask processing enables a robust estimate of the parameters since the inferior quality phase measurements would bias the linear fitting. Here, the parameters α and β for the Wenchuan PALSAR data were estimated to be -3.28×10^{-6} m^{-1} and -5.76×10^{-5} rad, respectively.

After estimating the parameters α and β, we used (3) to obtain the ionospheric phase by implementing an integration processing [21]. Note that the integral constant C in (3) should be carefully determined. The Wenchuan case's SAR data strip is long enough (nine frames), and more than three-fifths of the area is not seriously affected by coseismic displacement and large topographic relief. Therefore, we estimated the integral constant using the modified integral constant estimation (MICE) method proposed by Zhang *et al.* [21]. We first adopted the intensity cross-correlation method with a window size of 128 in range and 256 in azimuth to estimate the initial range displacements, and then, an iteration processing with a window size of 64 in range and 128 in azimuth to refine the initial range displacements. Afterward, the MICE method was introduced to calculate the integral constant [21]. Finally, we used (3) to estimate the ionospheric phase screen [see Fig. 3(b)] and remove it from the InSAR interferogram [see Fig. 3(c)].

To estimate the ionospheric phase using the RSS method, a bandpass filter with a bandwidth of one-third full bandwidth is adopted to divide the entire range spectrum of SAR images. The high- and low-frequency subband interferograms are then formed and used for ionospheric estimation. To reduce the influence of unwrapped error on the correction, we first masked the regions with coherence lower than 0.4. We then used a bilinear interpolation to fill out the masked areas. Besides, a spatial filter with window sizes of 128 was conducted to improve the phase quality further. The large filtering window would facilitate the removal of phase outlier, which may be significantly magnified by the large-scale factor of (6) [31]. After finishing the previous steps, the ionospheric phase screen [see Fig. 3(d)] and the corrected interferogram [see Fig. 3(e)] were generated.

This study obtained the ionospheric phase screens with the azimuth offset-based and RSS methods, respectively. Besides, we used the H-VCE algorithm to assign weights for the two groups of ionospheric phase screen, whose main steps have been described in Section II-C. The ionospheric phase screen estimated by the proposed method is depicted in Fig. 3(f). The corresponding corrected interferogram is presented in Fig. 3(g).

Fig. 3(c), (e), and (g) illustrates the azimuth offset-based, RSS, and integrated methods' corrected results, respectively. The results show that all the approaches can effectively remove ionospheric artifacts in InSAR interferograms. However, there are still significant residual errors in the nondeformable regions, both the corrected results of the azimuth offset-based and RSS methods, such as the regions 0 to 500th rows and 4000th to 5500th rows in Fig. 3(c) and (e). After the correction and implementing the proposed method, the residual errors have been greatly improved [see Fig. 3(g)], but it is still not perfect.

The ionospheric contribution extracted by the azimuth offset-based method, RSS method, and our proposed method to the InSAR phase varied from -27.0 to 14.4 rad, -15.1 to 12.6 rad, and -16.5 to 11.3 rad, respectively. These correspond to approximately 2.0 to -1.1 TECU, 1.1 to -0.9 TECU, and 1.2 to -0.9 TECU ionospheric disturbances along the LOS direction, respectively, equivalent to about -50.7 to 27.0 cm, 28.4 to 23.7 cm, and -31.0 to 21.1 cm of SAR range changes, respectively. It should be noted that the ionospheric contribution

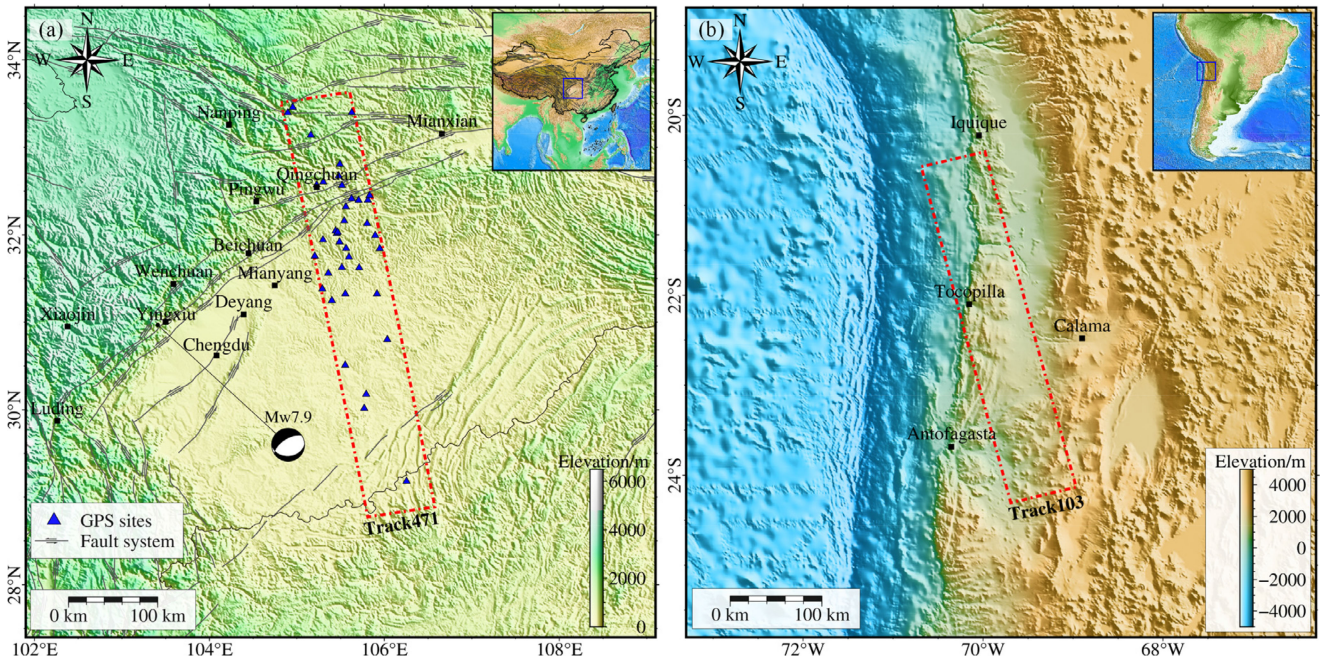

Fig. 2. Locations of the study sites. The red rectangles represent the footprints of ALOS PALSAR images covering (a) the Wenchuan earthquake and (b) a coastal region in Chile, respectively. The blue triangles and black lines in (a) represent the GPS sites and surface fault traces, respectively.

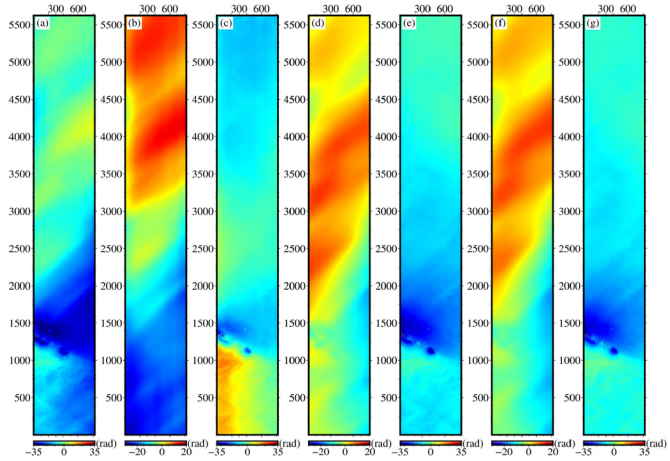

Fig. 3. (a) Original InSAR interferogram and the corrected interferograms from (c) the azimuth offset-based method, (e) the RSS method, and (g) the integrated correction method proposed in this study. The ionospheric phase screens estimated by the azimuth offset-based method, RSS method, and the proposed method are shown in (b), (d), and (f), respectively.

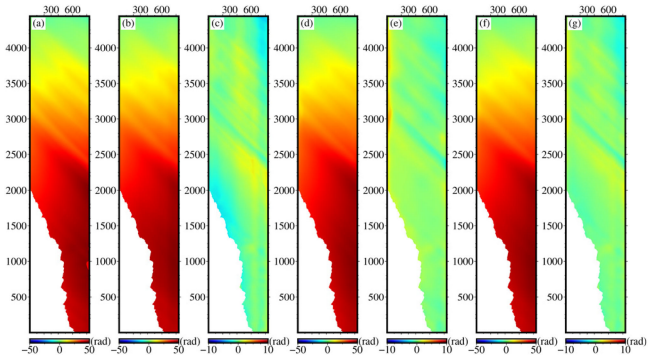

Fig. 4. Similar to Fig. 3, but for the PALSAR images covering the Chile case.

of the Wenchuan case extracted by the azimuth offset-based method is slightly different from the approach given by Zhang *et al.* [21]. This is probably because 1) we used more SAR images comparing with Zhang *et al.* [21], and 2) the processing parameters (e.g., multilooking number) are different as well.

B. Chile Test Case

We compared the Chile case with the Wenchuan case. We used the image pair of the track 103 in the Chile case with better coherence, and no significant deformation occurred during the image acquisition. The ionospheric phase screen was extracted by the azimuth offset-based method and is less affected by decorrelation and surface deformation. We applied similar Wenchuan case steps to obtain the ionospheric phase screen with the azimuth offset-based and RSS methods. The MAI interferogram and InSAR interferogram were multilooked by 6 × 30 looks in range and azimuth directions (∼ 95 × 95 m). Also, since the range bandwidth of the image pair is only half of that in the Wenchuan case, the larger spatial filter window size was adopted to smooth the ionospheric phase screen from the RSS method. Furthermore, we first masked the sea areas and low-coherence regions in the MAI interferogram, InSAR interferogram [see Fig. 4(a)], and range displacement map, and then interpolated the masked regions using an inpainting algorithm [38]. After the two steps, we calculated the ionospheric phase screen by using the azimuth offset-based method. Afterward, the locally move median filter with a window size of 40 × 40 pixels was used to remove the outliers in the interpolated range displacement field

map. The parameters α and β were estimated by using (1), and which are -1.56×10^{-4} m^{-1} and 1.05×10^{-4} rad, respectively. Considering that this image pair has no significant deformational signal, which means that we can ignore the aliasing of deformation and ionosphere. In addition, the SAR images of the Chile case were relatively of lower range resolution than the Wenchuan case, which means the lower accuracy of the MICE method to estimate the integral constant. We, therefore, used the differential averaging integral constant estimation (DAICE) method proposed by Jung *et al*. to calculate the integral constant [22].

Similar to the Wenchuan case, we applied the H-VCE algorithm described in Section II-C to combine the ionospheric phase screens generated by the azimuth offset-based and RSS methods. The InSAR interferograms were corrected by the azimuth offset-based, RSS, and the proposed methods shown in Fig. 4(c), (e), and (g), respectively. Fig. 4 depicts the estimated ionospheric phase screens using the azimuth offset-based [see Fig. 4(b)], RSS [see Fig. 4(d)], and the integrated methods [see Fig. 4(f)]. It shows that the ionospheric effect is about -2.5 to 50 rad along the LOS direction. This corresponds to about 0.2 to -3.8 TECU ionospheric interferences, which caused about -4.7 to 93.9 cm deformation errors along the LOS direction.

IV. Discussion

A. Key Factors for the Accuracy of the Proposed Method

The proposed method uses the H-VCE algorithm to assign the weights for the ionospheric phase screens of the azimuth offset-based and RSS methods to give full play to the two methods' advantages. Therefore, the proposed method's ionospheric estimation accuracy is closely related to the ionospheric estimation accuracy of the two methods separately. The integral constant is an essential factor in determining the ionospheric estimation accuracy of the azimuth offset-based method. While the RSS method's ionospheric estimation accuracy mainly depends on the coherence of image pair and the range bandwidth of the SAR system [21], [24].

The integral operation significantly limits the azimuth offset-based method's sensitivity to the long-wavelength ionosphere [25], [30], which is closely related to the integral constant. The common estimation (i.e., DAICE) method of the integral constant is based on the assumed correlation between the ionospheric phase screen and InSAR phase [21], [22].The integral constant is calculated by averaging the difference between ionospheric phase screen estimator and the InSAR phase [21], [22]. However, this method is challenging to distinguish the ionospheric components from large ground displacements [39]. The MICE method estimated the integral constant using the principle that signal group delay and phase advance are equal in magnitude and opposite in sign to combine the azimuth displacements and range displacements [21]. This method can effectively reduce the influence of surface deformation on the ionospheric phase screen estimation. Still, its accuracy depends on the length of the data strips and the range resolution of the SAR image, which is almost unaffected by large ground deformation or substantial topography [21].

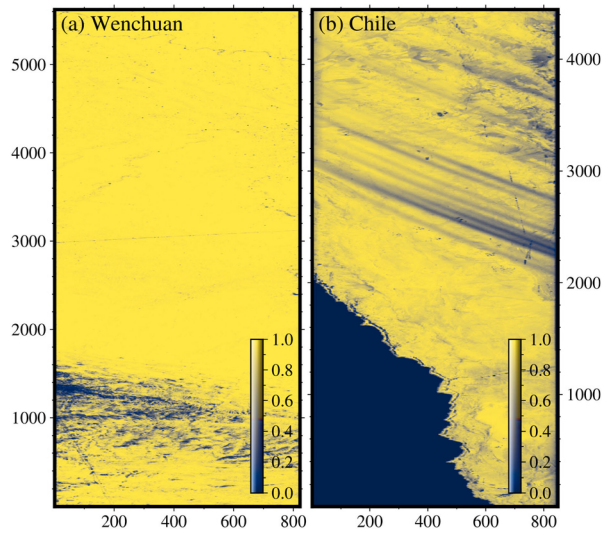

Fig. 5. Interferometric coherence maps for (a) the Wenchuan case (b) and Chile case.

For the Wenchuan case, more than three-fifths of the regions are not seriously affected by the coseismic deformation and topographic relief. Therefore, the MICE method was used to calculate the integral constants in this study, and it presented a strong performance in removing the long-wavelength ionospheric errors [see Fig. 5(b)]. In contrast, the image pair in the Chile case with high coherence and no significant surface deformation during image acquisition [39]. Unfortunately, the upper left regions of the images connect with the ocean [see Fig. 2(b)], which results in that the length of the data strip cannot support the accurate estimation of the integral constant with the MICE method [21]. Additionally, the range resolution of the SAR images is only about half of the Wenchuan case, which limits the obtaining of sufficiently accurate range displacements to implement the MICE method. We, therefore, adopted the DAICE approach instead of the MICE method.

The estimated ionospheric phase screen from the RSS method is essentially a linear combination of different interferograms multiplied by corresponding scale factors (6). Therefore, the accuracy of this method is closely related to the phase quality and scale factor. However, the phase quality depends on the coherence, and the scale factor depends on the range bandwidth. When the coherence is low, decorrelation and phase unwrapping errors are larger, and the phase quality is low; otherwise, it is vice versa. Additionally, small range bandwidth can cause a large-scale factor, which amplifies all kinds of errors. When the scale factor is significant, a large spatial filtering window size is often needed to smooth the ionospheric phase screen estimated by the RSS method [24], [39]. This means that image resolution is lost, and sensitivity to the small-scale ionospheric variations is reduced [30], [39].

The two cases in this study are both with high coherence, and the coherence maps of the Wenchuan case and Chile case are shown in Fig. 5(a) and (b), respectively. The mean coherences of the two cases are more than 0.5, which means the phase unwrapping is performed without problems [24]. However, the range

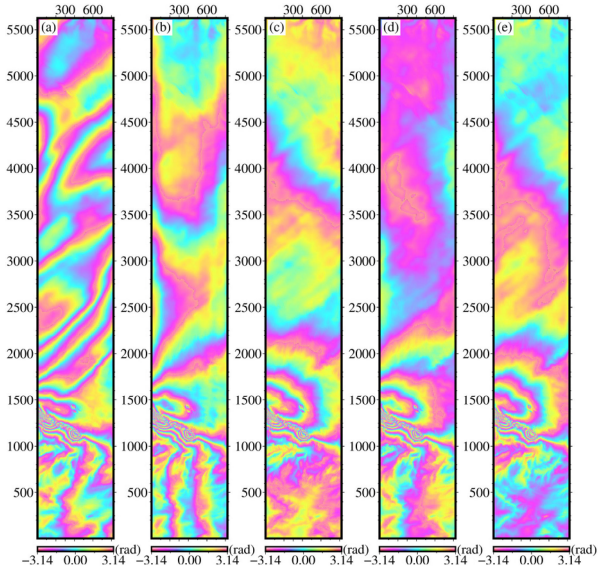

Fig. 6. Rewrapped PALSAR interferograms of the Wenchuan earthquake. (a) Original differential SAR interferogram and the corrected interferograms from (b) the azimuth offset-based method, (c) the RSS method, (d) the equal weight least squares method, and (e) the proposed method.

bandwidth of the SAR data in the Wenchuan case is 28 MHz, whereas Chile is 14 MHz. The corresponding largest scale factors are about −34.02 for the Wenchuan case and −68.04 for Chile. Therefore, the RSS method's implementation needed spatial filtering with a large window size to denoise and removed outliers in the two cases. It means that the ionospheric phase screen maps' resolution is lost, and the small-scale ionospheric variations are difficult to estimate, especially in the Chilean case.

B. Comparison of Different Methods

To facilitate comparative analysis of the proposed method's corrected result, we rewrapped the interferograms of the Wenchuan case obtained from the results of the original, the azimuth offset-based method, RSS method, weighted least squares method, and our method. The rewrapped interferograms are shown in Fig. 6(a)–(e), respectively. Comparing the results in Fig. 6(a) with the results in Fig. 6(b)–(e), we found that the ionospheric streaks have been effectively removed, and the coseismic deformation field was recovered after ionospheric correction with the four methods mentioned earlier. However, after the correction and implementation of the azimuth offset-based method, there are still significant streaks along the azimuth direction, and only a complete phase circle was recovered [see Fig. 6(b)]. It may be mainly due to the corrected interferogram contained the integral constant errors and residual orbital errors. In contrast, the RSS method has recovered three complete phase circles, but azimuth streak still presents in the region between 3000th and 4500th in Fig. 6(c), and some patchy phases present in the region between 3500th and 5600th in Fig. 6(c). These two types of errors are likely caused by uncompensated orbit and small-scale ionospheric variations.

Moreover, although the weighted least squares method can give play to the advantages of the azimuth offset-based and RSS methods to some extent, the result is not ideal because of the inaccurate weights [see Fig. 6(d)]. After ionospheric correction using the proposed method, the patchy phases present in the region between 3500th and 5600th in Fig. 6(c) were removed, and three complete phase circles were recovered simultaneously [see Fig. 6(e)]. However, the azimuth fringe that appears in Fig. 6(c) still exists in Fig. 6(e), which is mainly residual orbital errors.

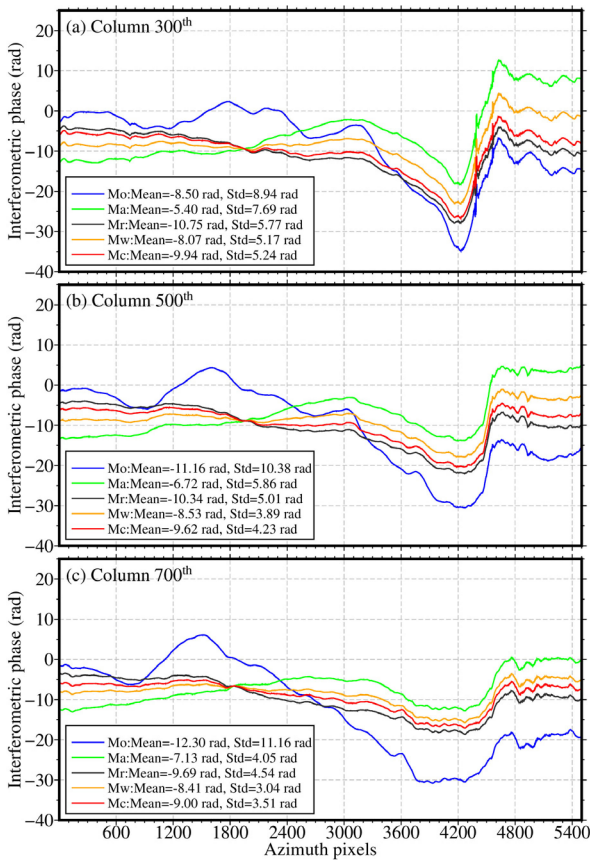

Fig. 7. Variations in the unwrapped phase along with the three-column profiles before and after ionospheric phase correction, i.e., (a) 300th, (b) 500th, and (c) 700th column. The blue, green, gray, orange, and red lines represent the uncorrected phase (Mo), and those corrected from the azimuth offset-based method (Ma), RSS method (Mr), weighted least squares method (Mw), and joint correction method (Mc), respectively.

For the Chile case, the azimuth offset-based and RSS methods' correction results are basically the same. However, there are still some differences in local areas, especially the interferograms' edges and the areas connected to the ocean [see Fig. 4(c) and (e)]. The results have been greatly improved by using the proposed method [see Fig. 4(g)]. Nevertheless, there are still some uncertain errors, which we suspect may be mainly the tropospheric and residual orbital errors.

To better compare the phase changes along the azimuth direction of the corrected results obtained from the four different methods, we extracted three profile lines (i.e., column 300th, 500th, and 700th) from the original and corrected interferograms in the Wenchuan case, and the results are shown in Fig. 7(a)–(c), respectively. Results show that interferometric phases of the three profile lines are more flattened in the far-field. It also

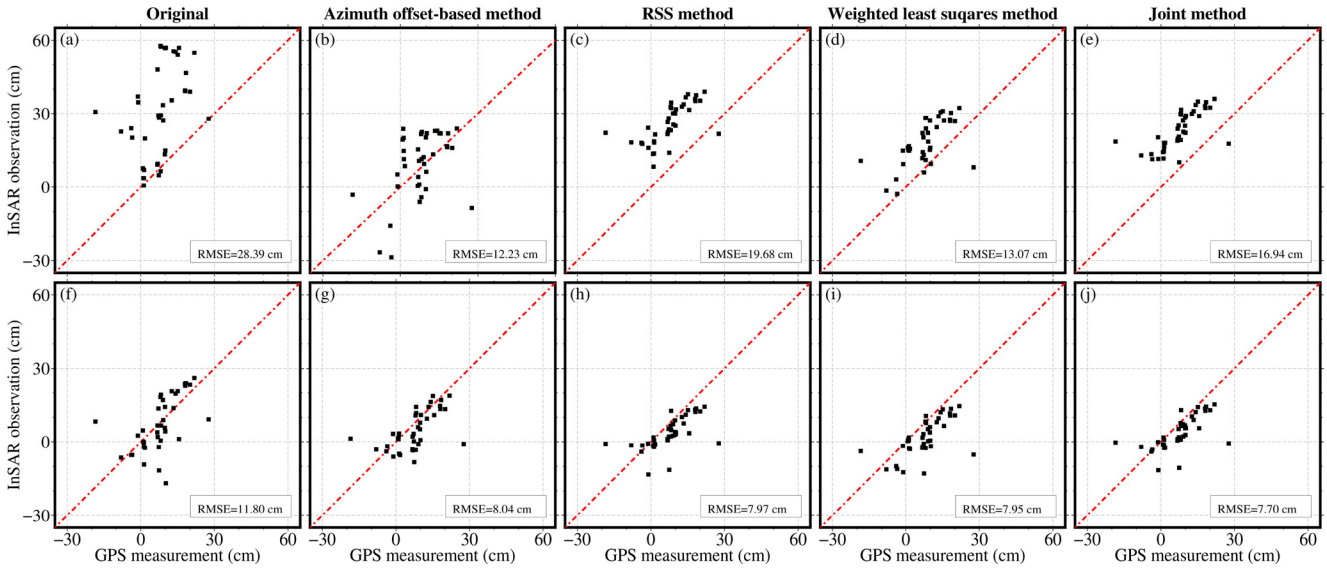

Fig. 8. Cross plots of GPS measurements and (a) the original uncorrected InSAR measurements, (b) the corrected results with the azimuth offset-based method, (c) the corrected results with the RSS method, and (d) the corrected results with the proposed method. The InSAR measurements in (a)–(e) are not only corrected for ionospheric phase but also for residual errors with a quadratic polynomial fitting, whereas in plots (f)–(j), the residual errors are not corrected.

reveals that the phase standard deviations decreased significantly after ionospheric correction with the four correction methods. The corrected results after ionospheric correction with the azimuth offset-based method (green lines) are considerably lower than the other results from the phase's absolute value. This is likely to say that the estimated integral constants were still mixed with other nonionospheric terms and removed from the interferometric phases as a part of the ionospheric phase screen.

Moreover, the standard deviations of the weighted least squares method (orange lines) are markedly lower than that of other methods. This is because we assigned equal weights to the azimuth offset-based and RSS methods, which generally made the interferometric phases smoother and increased the local errors due to the unreasonable weights. In fact, after ionospheric correction with the RSS method (gray lines), the deformation field is consistent with that published in [40], which verified to be close to GPS observations. Nevertheless, the residual orbital errors and small-scale ionospheric disturbances still exist [e.g., in the region between 3500th and 5600th in Fig. 6(c)]. Our method results are relatively close to those of the RSS method, but the former's standard deviations are significantly lower than that of the latter. This is because the H-VCE algorithm can accurately weigh the azimuth offset-based and RSS methods. This proposed method can simultaneously compensate for the small-scale ionospheric disturbances and remove the long-wavelength ionospheric errors. Unfortunately, after ionospheric correction with the RSS method, the weighted least squares method, and the proposed method, although the corrected interferometric phases changed more flattened in the far-field, there are still relatively stable phase deviations between the corrected interferometric phases and zero, which may be mainly caused by the nonionospheric phase terms, such as residual orbital errors and coregistered offset ramp [20].

C. Comparison to GPS Measurement

To quantitatively evaluate the accuracy and reliability of the proposed method, we used the 3-D (east, north, and up) displacements before and after the Wenchuan earthquake measured by 39 available GPS sites [see the blue triangles in Fig. 2(a)] given in Wang *et al.* as the truth ground displacements [41]. To facilitate a comparison of the displacements between GPS and InSAR, we projected the GPS displacements into the InSAR LOS direction based on the geometry of SAR observations. The comparison between GPS-derived and InSAR LOS displacements is shown in Fig. 8. The comparative results of the original interferogram, interferogram after ionospheric correction with the azimuth offset-based method, interferogram after ionospheric correction with the RSS method, interferogram after ionospheric correction with the weighted least squares method, and interferogram after ionospheric correction with the integrated method are presented in Fig. 8(a)–(e), respectively. As shown in Fig. 8(a), the root-mean-squared error (RMSE) between the GPS and the original InSAR LOS displacements is 28.39 cm. After ionospheric correction with the azimuth offset-based method, RSS method weighted least squares method, and the proposed method, the RMSEs decreased to 12.23, 19.68, 13.07, and 16.94 cm, respectively, which indicate that the four methods can effectively alleviate ionospheric artifacts. However, there is a relatively fixed deviation between the results corrected by the RSS method and the GPS measurements, which leads to a similar situation for the weighted least squares method and the proposed method due to the weighting process. This is consistent with the results shown in Fig. 7, which has been interpreted to be caused by the nonionospheric phase terms. The accuracy of the azimuth offset-based method is the highest due to part of nonionospheric phases averaged into the integral constant and corrected as the ionospheric phase.

We used the quadratic polynomial to fit the residual errors and subtract them from the original interferometric phases and the interferometric phases after ionospheric correction to verify this interpretation. The corresponding results are shown in Fig. 8(f)–(j), respectively. After the residual error correction, we found that the fixed deviations described earlier have been significantly mitigated, where the RMSEs of the RSS method, weighted least squares method, and the integrated method decreased to 7.97, 7.95, and 7.70 cm, respectively. These, on the one hand, prove our previous suspicions to be correct, and on the other hand, demonstrate the proposed method's effectiveness. Moreover, after the correction for the residual errors with the quadratic polynomial, the most significant drop of RMSE is the original interferogram. In comparison, the smallest drop of RMSE is the interferogram with ionospheric correction when we used the azimuth offset-based method. Comparing the RMSEs before and after the quadratic polynomial correction shows the necessity of the residual error correction. It also proves that the integral constant mixed with the nonionospheric component to some extent. Furthermore, after the two corrections, there are still some differences between the InSAR and GPS displacements, mainly due to the different temporal coverage between GPS and InSAR data.

V. Conclusion

We presented an integrated method that combines the ionospheric measurements obtained from the azimuth offset-based method and the RSS method based on the H-VCE algorithm to improve the ionospheric phase correction accuracy for InSAR. The ALOS-1 PALSAR images acquired along track 471, covering the 2008 Wenchuan (Mw 7.9) earthquake and along-track 103, covering the north of Chile with no significant deformation, were used to test the integrated method. The two tested results show that the integrated method can be effectively used to correct the long-wavelength ionospheric component and local scale ionospheric disturbances. The Wenchuan case proved the integrated method could successfully recover the deformation fringes near the fault without apparent cumulative error.

The proposed method provides a new idea for combining different ionospheric correction methods. Our proposed method is effective in correcting in correcting both long-wavelength ionospheric components and local ionospheric disturbances. However, phase ramps in the MAI interferogram due to the baseline difference between forward- and backward-looking interferograms may still retain. Further corrections are thus needed to eliminate these errors. Moreover, our method is only a weighted method among different data groups, which has no practical physical meaning. Therefore, the proposed method still has some shortcomings. Therefore, we suggest developing a new method for InSAR ionospheric correction in future studies.

Acknowledgment

The authors would like to thank the Japanese Aerospace Exploration Agency (JAXA) for providing the ALOS-1 PALSAR level 1.0 SAR data and the reviewers for their valuable comments and suggestions to improve the quality of this article. Figs. 2–8 were generated by the Generic Mapping Tool software [42].

References

[1] A. Hooper, D. Bekaert, K. Spaans, and M. Arıkan, "Recent advances in SAR interferometry time series analysis for measuring crustal deformation," *Tectonophysics*, vol. 514–517, pp. 1–13, 2012.

[2] J. Li, Z. Li, X. Ding, Q. Wang, J. Zhu, and C. Wang, "Investigating mountain glacier motion with the method of SAR intensity-tracking: Removal of topographic effects and analysis of the dynamic patterns," *Earth Sci. Rev.*, vol. 138, pp. 179–195, 2014.

[3] T. Strozzi *et al.*, "Estimation of Arctic glacier motion with satellite L-band SAR data," *Remote Sens. Environ.*, vol. 112, no. 3, pp. 636–645, Mar. 2008.

[4] T. Strozzi, A. Luckman, T. Murray, U. Wegmuller, and C. L. Werner, "Glacier motion estimation using SAR offset-tracking procedures," *IEEE Trans. Geosci. Remote Sens.*, vol. 40, no. 11, pp. 2384–2391, Nov. 2002.

[5] K. A. C. de Macedo, F. L. G. Ramos, C. Gaboardi, J. R. Moreira, F. Vissirini, and M. S. da Costa, "A compact ground-based interferometric radar for landslide monitoring: The Xerém experiment," *IEEE J. Sel. Topics Appl. Earth Observ. Remote Sens.*, vol. 10, no. 3, pp. 975–986, Mar. 2017.

[6] D. Perissin and T. Wang, "Time-series InSAR applications over urban areas in China," *IEEE J. Sel. Topics Appl. Earth Observ. Remote Sens.*, vol. 4, no. 1, pp. 92–100, Mar. 2011.

[7] D. Massonnet and K. L. Feigl, "Radar interferometry and its application to changes in the Earth's surface," *Rev. Geophys.*, vol. 36, no. 4, pp. 441–500, Nov. 1998.

[8] M. Chini *et al.*, "The May 12, 2008, (Mw 7.9) Sichuan earthquake (China): Multiframe ALOS-PALSAR DInSAR analysis of coseismic deformation," *IEEE Geosci. Remote Sens. Lett.*, vol. 7, no. 2, pp. 266–270, Apr. 2010.

[9] D. Poreh and S. Pirasteh, "InSAR observations of the Medicina Geodetic Observatory and CosmoSKYMed images analysis," *Nat. Hazards*, vol. 103, no. 3, pp. 3145–3161, 2020.

[10] C. Carnec and H. Fabriol, "Monitoring and modeling land subsidence at the Cerro Prieto Geothermal Field, Baja California, Mexico, using SAR interferometry," *Geophys. Res. Lett.*, vol. 26, no. 9, pp. 1211–1214, 1999.

[11] H. S. Jung, Z. Lu, J. S. Won, M. P. Poland, and A. Miklius, "Mapping three-dimensional surface deformation by combining multiple-aperture interferometry and conventional interferometry: Application to the June 2007 eruption of Kilauea Volcano, Hawaii," *IEEE Geosci. Remote Sens. Lett.*, vol. 8, no. 1, pp. 34–38, Jan. 2011.

[12] F. Meyer, R. Bamler, N. Jakowski, and T. Fritz, "The potential of low-frequency SAR systems for mapping ionospheric TEC distributions," *IEEE Geosci. Remote Sens. Lett.*, vol. 3, no. 4, pp. 560–564, Oct. 2006.

[13] P. A. Rosen, S. Hensley, and C. Chen, "Measurement and mitigation of the ionosphere in L-band interferometric SAR data," in *Proc. IEEE Radar Conf.*, May 2010, pp. 1459–1463.

[14] R. Brcic, A. Parizzi, M. Eineder, R. Bamler, and F. Meyer, "Estimation and compensation of ionospheric delay for SAR interferometry," in *Proc. Int. Geosci. Remote Sens. Symp.*, Jul. 2010, pp. 2908–2911.

[15] J. S. Kim, A. Danklmayer, and K. Papathanassiou, "Correction of ionospheric distortions in low-frequency interferometric SAR data," in *Proc. Int. Geosci. Remote Sens. Symp.*, Jul. 2011, pp. 1505–1508.

[16] J. Li, Y. Ji, Y. Zhang, Q. Zhang, and Z. Dong, "Effects of ionosphere polarimetric dispersion on lower-frequency spaceborne SAR," in *Proc. IEEE 3rd Int. Conf. Signal Image Process.*, 2018, pp. 510–515.

[17] M. Jehle, M. Ruegg, L. Zuberbuhler, D. Small, and E. Meier, "Measurement of ionospheric Faraday rotation in simulated and real spaceborne SAR data," *IEEE Trans. Geosci. Remote Sens.*, vol. 47, no. 5, pp. 1512–1523, May 2009.

[18] J. S. Kim, K. P. Papathanassiou, R. Scheiber, and S. Quegan, "Correcting distortion of polarimetric SAR data induced by ionospheric scintillation," *IEEE Trans. Geosci. Remote Sens.*, vol. 53, no. 12, pp. 6319–6335, Dec. 2015.

[19] F. Meyer and J. Nicoll, "Prediction, detection, and correction of Faraday rotation in full-polarimetric L-band SAR data," *IEEE Trans. Geosci. Remote Sens.*, vol. 46, no. 10, pp. 3076–3086, Oct. 2008.

[20] D. Raucoules and M. De Michele, "Assessing ionospheric influence on L-band SAR data: Implications on coseismic displacement measurements of the 2008 Sichuan earthquake," *IEEE Geosci. Remote Sens. Lett.*, vol. 7, no. 2, pp. 286–290, Apr. 2010.

[21] B. Zhang, X. Ding, W. Zhu, C. Wang, L. Zhang, and Z. Liu, "Mitigating ionospheric artifacts in coseismic interferogram based on offset field

derived from ALOS-PALSAR data," *IEEE J. Sel. Topics Appl. Earth Observ. Remote Sens.*, vol. 9, no. 7, pp. 3050–3059, Jul. 2016.
[22] H. S. Jung, D. T. Lee, Z. Lu, and J. S. Won, "Ionospheric correction of SAR interferograms by multiple-aperture interferometry," *IEEE Trans. Geosci. Remote Sens.*, vol. 51, no. 5, pp. 3191–3199, May 2013.
[23] Z. Liu, H. Jung, and Z. Lu, "Joint correction of ionosphere noise and orbital error in L-Band SAR interferometry of interseismic deformation in Southern California," *IEEE Trans. Geosci. Remote Sens.*, vol. 52, no. 6, pp. 3421–3427, Jun. 2014.
[24] G. Gomba, A. Parizzi, F. De Zan, M. Eineder, and R. Bamler, "Toward operational compensation of ionospheric effects in SAR interferograms: The split-spectrum method," *IEEE Trans. Geosci. Remote Sens.*, vol. 54, no. 3, pp. 1446–1461, Mar. 2016.
[25] G. Gomba and F. De Zan, "Bayesian data combination for the estimation of ionospheric effects in SAR interferograms," *IEEE Trans. Geosci. Remote Sens.*, vol. 55, no. 11, pp. 6582–6593, Nov. 2017.
[26] G. Gomba, F. R. González, and F. De Zan, "Ionospheric phase screen compensation for the Sentinel-1 TOPS and ALOS-2 ScanSAR modes," *IEEE Trans. Geosci. Remote Sens.*, vol. 55, no. 1, pp. 223–235, Jan. 2017.
[27] M. Furuya, T. Suzuki, J. Maeda, and K. Heki, "Midlatitude sporadic-E episodes viewed by L-band split-spectrum InSAR," *Earth, Planets, Space*, vol. 69, no. 1, 2017, Art. no. 175.
[28] C. Liang, P. Agram, M. Simons, and E. J. Fielding, "Ionospheric correction of InSAR time-series analysis of C-band Sentinel-1 TOPS data," *IEEE Trans. Geosci. Remote Sens.*, vol. 57, no. 9, pp. 6755–6773, Sep. 2019.
[29] H. Liao, F. J. Meyer, B. Scheuchl, J. Mouginot, I. Joughin, and E. Rignot, "Ionospheric correction of InSAR data for accurate ice velocity measurement at polar regions," *Remote Sens. Environ.*, vol. 209, pp. 166–180, May 2018.
[30] G. Gomba, F. De Zan, and A. Parizzi, "Ionospheric phase screen and ionospheric azimuth shift estimation combining the split spectrum and multi-squint methods," in *Proc. 11th Eur. Conf. Synth. Aperture Radar*, Jun. 2016, pp. 1–4.
[31] U. Wegmüller, C. Werner, O. Frey, C. Magnard, and T. Strozzi, "Reformulating the split-spectrum method to facilitate the estimation and compensation of the ionospheric phase in SAR interferograms," *Procedia Comput. Sci.*, vol. 138, pp. 318–325, 2018.
[32] K. Hasni, J. Chen, and L. Zhuo, "A refined split-spectrum algorithm for correcting ionospheric effects on interferograms of spaceborne D-InSAR at longer wavelength," in *Proc. Int. Geosci. Remote Sens. Symp.*, Jul. 2016, pp. 6855–6858.
[33] J. H. Liu, J. Hu, Z. W. Li, J. J. Zhu, Q. Sun, and J. Gan, "A method for measuring 3-D surface deformations with InSAR based on strain model and variance component estimation," *IEEE Trans. Geosci. Remote Sens.*, vol. 56, no. 1, pp. 239–250, Jan. 2017.
[34] J. Hu, Z. W. Li, Q. Sun, J.-J. Zhu, and X.-L. Ding, "Three-dimensional surface displacements from InSAR and GPS measurements with variance component estimation," *IEEE Geosci. Remote Sens. Lett.*, vol. 9, no. 4, pp. 754–758, Jul. 2012.
[35] U. Wegmüller and C. Werner, "Gamma SAR processor and interferometry software," in *Proc. Eur. Space Agency Spec. Publ.*, 1997, pp. 1687–1692.
[36] R. M. Goldstein and C. L. Werner, "Radar interferogram filtering for geophysical applications," *Geophys. Res. Lett.*, vol. 25, no. 21, pp. 4035–4038, 1998.
[37] C. W. Chen and H. A. Zebker, "Two-dimensional phase unwrapping with use of statistical models for cost functions in nonlinear optimization," *J. Opt. Soc. Amer. A Opt. Image Sci.*, vol. 18, no. 2, pp. 338–351, 2001.
[38] J. D'Errico, *MATLAB Central File Exchange*, inpaint_nans, 2020. Retrieved: Oct. 4, 2020. [Online]:Available: https://www.mathworks.com/matlab central/fileexchange/4551-inpaint_nans
[39] H. Fattahi, M. Simons, and P. Agram, "InSAR time-series estimation of the ionospheric phase delay: An extension of the split range-spectrum technique," *IEEE Trans. Geosci. Remote Sens.*, vol. 55, no. 10, pp. 5984–5996, Oct. 2017.
[40] G. Feng, S. Jónsson, and Y. Klinger, "Which fault segments ruptured in the 2008 Wenchuan earthquake and which did not? New evidence from near-fault 3D surface displacements derived from SAR image offsets," *Bull. Seismological Soc. Amer.*, vol. 107, no. 3, pp. 1185–1200, 2017.
[41] Q. Wang *et al.*, "Rupture of deep faults in the 2008 Wenchuan earthquake and uplift of the Longmen Shan," *Nat. Geosci.*, vol. 4, pp. 634–640, 2011.
[42] P. Wessel *et al.*, "The generic mapping tools version 6," *Geochem., Geophys., Geosystems*, vol. 20, no. 11, pp. 5556–5564, 2019.

Wenfei Mao received the B.Eng. and M.Eng. degrees in surveying engineering from the East China University of Technology, Fuzhou, China, in 2013 and 2018, respectively. Since 2018, he has been working toward the Ph.D. degree in photogrammetry and remote sensing the Faculty of Geosciences and Environmental Engineering, Southwest Jiaotong University, Chengdu, China.

His current research interests include ionospheric modeling and correcting for InSAR/TS-InSAR based on GNSS and SAR, and geological hazard monitoring.

Guoxiang Liu received the B.Eng. degree in surveying engineering from the East China Institute of Geology, Fuzhou, China, in 1991, the M.Eng. degree in geomatics from the Southwest Jiaotong University, Chengdu, China, in 1994, and the Ph.D. degree in remote sensing from The Hong Kong Polytechnic University, Hong Kong, in 2003.

He is currently a Professor with the Department of Remote Sensing and Geospatial Information Engineering, Southwest Jiaotong University. From 2005 to 2006, he was a Visiting Scholar and conducted research on InSAR with Dr. S. M. Buckley with the Department of Aerospace Engineering and Engineering Mechanics, The University of Texas at Austin, Austin, TX, USA. He is author of three books, more than 170 articles, and holds 12 patents. His current research interests include InSAR, PSI, radargrammetry, and digital photogrammetry for regional mapping topography, and deformation.

Prof. Liu was a Co-Chair of the Working Group VII of the ISPRS Technical Commission VII and a member of the Commission on Mapping from Satellite Imagery of the International Cartographic Association.

Xiaowen Wang received the B.S. degree in geomatics from Henan Polytechnic University, Jiaozuo, China, in 2010, and the Ph.D. degree in photogrammetry and remote sensing from Southwest Jiaotong University, Chengdu, China, in 2017.

He is currently an Associate Professor with the Faculty of Geosciences and Environmental Engineering, Southwest Jiaotong University, where he is mainly involved in crustal deformation measuring and modeling using remote sensing techniques, such as interferometric synthetic aperture radar, optical image cross-correlation, and digital elevation model differencing.

Rui Zhang received the B.Eng. degree in mechanical engineering from the North China University of Water Resources and Electric Power, Henan, China, in 2004, and the M.Eng. degree in geographic information engineering and the Ph.D. degree in remote sensing from the Southwest Jiaotong University, Chengdu, China, in 2008 and 2012, respectively.

He is currently an Associate Professor with the Faculty of Geosciences and Environmental Engineering, Southwest Jiaotong University. From 2012 to 2014, he was a Postdoctoral Fellow with The Institute of Space and Earth Information Science, The Chinese University of Hong Kong, Hong Kong. His research interests include the development of ground deformation monitoring and early warning system, fundamental study of microware remote sensing, and synthetic aperture radar interferometry.

Prof. Zhang was a recipient of the Best Paper Award of the 2nd International Workshop on Earth Observation and Remote Sensing Application, in 2012, and the Annual Excellent Paper Award of the Journal of Remote Sensing, in 2019.

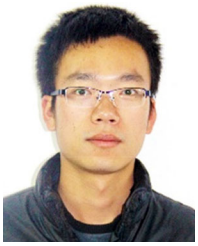

Wei Xiang received the B.Eng. and M.Eng. degrees in surveying engineering from the China University of Geosciences, Wuhan, China, in 2012 and 2014, respectively. Since 2017, he has been working toward the Ph.D. degree in photogrammetry and remote sensing with the Faculty of Geosciences and Environmental Engineering, Southwest Jiaotong University, Chengdu, China.

His current research interests include geological hazard monitoring and time-series InSAR.

Shuaiying Wu received the B.S. degree in surveying and mapping engineering from the East China University of Technology, Fuzhou, China, in 2009, and the M.S. degree in photogrammetry and remote sensing from Southwest Jiaotong University, Chengdu, China, in 2012. She is currently working toward the Ph.D. degree in photogrammetry and remote sensing with the Faculty of Geosciences and Environmental Engineering, Southwest Jiaotong University, where she is mainly involved in groundwater monitoring combined with various remote-sensing methods InSAR, GRACE, and GPS.

Bo Zhang received the B.S. and M.S. degrees in surveying engineering and disaster prevention and mitigation engineering, in 2010 and 2014, respectively, from the Southwest Jiaotong University, Chengdu, China, where he is currently working toward the Ph.D. degree in photogrammetry and remote sensing with the Faculty of Geosciences and Environmental Engineering.

His current research interests include radar interferometry and remote sensing glaciology.

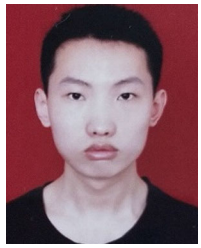

Jiawen Bao received the B.S. degree in remote sensing science and technology from the School of Remote Sensing and Information Engineering, Wuhan University, Wuhan, China, in 2014. He has been working toward the Ph.D. degree in photogrammetry and remote sensing with the Faculty of Geosciences and Environmental Engineering, Southwest Jiaotong University, Chengdu, China, since 2015.

His current research interests include radar interferometry and time-series displacement monitoring.

Jialun Cai received the B.Eng. and M.Eng. degrees in surveying engineering and mineral prospecting and exploration from the Southwest University of Science and Technology, Miangyang, China, in 2013 and 2016, respectively. Since 2016, he has been working toward the Ph.D. degree in photogrammetry and remote sensing with the Faculty of Geosciences and Environmental Engineering, Southwest Jiaotong University, Chengdu, China.

His current research interests include geological hazard monitoring, InSAR, ground-based SAR, and UAV aerial photogrammetry.

Saeid Pirasteh received the Ph.D. degree in geology (remote sensing and GIS) from Aligarh Muslim University, Aligarh, India, in 2004, and the Ph.D. degree in geography (GIS, geoanalytics, and LiDAR) from the University of Waterloo, Waterloo, ON, Canada, in 2018.

He is currently an Associate Professor with the Faculty of Geosciences and Environmental Engineering, Southwest Jiaotong University, Chengdu, China. His research interests include remote sensing and LiDAR data processing and geology applications, environmental hazards, and disaster assessment toward implementing UN sustainable development goals 2030. He is also interested in integrating artificial intelligence, machine learning, computer vision, development of geospatial algorithms, models, software, mobile, and web app in geosciences applications.

Dr. Pirasteh is the UN-GGIM Academic Network Member.